Tensor-based analysis of the flow topology in droplet-laden homogeneous isotropic turbulence

By M. S. Dodd AND L. Jofre

1. Motivation and objectives

Turbulence modeling in dispersed multiphase flows remains an outstanding challenge, especially when the dispersed phase has characteristic sizes larger than the smallest length scales of the flow, rendering a point particle approximation inaccurate. For finite-size droplets and particles, it is unclear whether the small scales are universal and statistically isotropic. In particular, a question arises concerning how the structure of the turbulence changes with respect to distance from the dispersed phase.

The purpose of this study is to investigate the small-scale flow topology in droplet-laden decaying isotropic turbulence using tensor-based analysis of the velocity gradient. We compute the invariants of the velocity-gradient, rate-of-strain, and rate-of-rotation tensors for a direct numerical simulation (DNS) dataset. The Taylor-scale Reynolds number at the time of droplet release is $Re_\lambda = 83$, the density and viscosity ratio of the droplet to carrier fluid are both 10, and the Weber number of the droplets based on the root-mean-square (r.m.s.) velocity of turbulence is $We_{\mathrm{rms}} = 1$. Volume-of-fluid (VoF) and level-set (LS) fields are used to capture the motion of the droplet interface. To quantify how the fine-scale motions change with respect to proximity to the droplet surface, the LS (signed-distance) function is used to condition the dissipation rate of turbulence kinetic energy (TKE) and the joint probability density function (PDF) of the velocity-gradient invariants.

2. Theoretical background

The use of DNS to study the velocity-gradient statistics in turbulent flows has a long history. Most analyses of velocity-gradient statistics have been confined to single-phase flows. The field of research that connected invariants of the velocity-gradient tensor to flow topologies was initiated by Chong *et al.* (1990). They employed critical point theory to relate the invariants of the velocity-gradient tensor to the local three-dimensional flow field as seen by an observer traveling with the local velocity of the flow.

2.1. *Invariants of the velocity-gradient tensor*

The velocity-gradient tensor $A_{ij} \equiv \partial u_i/\partial x_j$ can be decomposed into symmetric and skew-symmetric parts. The symmetric part is the rate-of-strain tensor

$$S_{ij} \equiv \frac{1}{2}\left(\frac{\partial u_i}{\partial x_j} + \frac{\partial u_j}{\partial x_i}\right), \tag{2.1}$$

and the skew-symmetric part is the rate-of-rotation tensor

$$\Omega_{ij} \equiv \frac{1}{2}\left(\frac{\partial u_i}{\partial x_j} - \frac{\partial u_j}{\partial x_i}\right), \tag{2.2}$$

such that $A_{ij} = S_{ij} + \Omega_{ij}$.

In incompressible flow, the pressure p satisfies the Poisson equation $\nabla^2 p = -\rho A_{ij} A_{ji}$, which can be written in terms of S_{ij} and Ω_{ij} as $\nabla^2 p = \rho(\Omega_{ij}\Omega_{ij} - S_{ij}S_{ij})$, and reformulated in terms of the local dissipation rate of TKE ($\varepsilon' \equiv 2\nu S_{ij}S_{ij}$) and enstrophy ($\omega' \equiv 2\Omega_{ij}\Omega_{ij}$) as

$$\nabla^2 p = \frac{\rho}{2}\left(\omega - \frac{\varepsilon}{\nu}\right). \tag{2.3}$$

The coefficients of the characteristic equation of A_{ij}, written as

$$\lambda_i^3 + P_A \lambda_i^2 + Q_A \lambda_i + R_A = 0, \tag{2.4}$$

are the tensor invariants, which, for incompressible flow ($\nabla \cdot \mathbf{u} = 0$), are given by

$$P_A = -\mathrm{tr}(\mathbf{A}) = -A_{ii} = 0, \tag{2.5}$$

$$Q_A = -\frac{1}{2}\mathrm{tr}(\mathbf{A}^2) = -\frac{1}{2}A_{ij}A_{ji} = \frac{1}{2}(\Omega_{ij}\Omega_{ij} - S_{ij}S_{ij}) = \frac{1}{4}\left(\omega' - \frac{\varepsilon'}{\nu}\right), \tag{2.6}$$

$$R_A = -\frac{1}{3}\mathrm{tr}(\mathbf{A}^3) = -\frac{1}{3}A_{ij}A_{jk}A_{ki}. \tag{2.7}$$

The tensor invariants for S_{ij} and Ω_{ij} can be defined in a similar manner. Due to incompressibility, $P_A = P_S = P_\Omega = 0$ and, due to Ω_{ij} being skew-symmetric, $R_\Omega = -\det(\Omega_{ij}) = 0$. The local dissipation rate of TKE can be written in terms of Q_S as

$$\varepsilon = -4\nu Q_S, \tag{2.8}$$

and the enstrophy can be written in terms of Q_Ω as

$$\omega = 4Q_\Omega. \tag{2.9}$$

3. Numerical simulation and flow properties

This study uses results from DNS of droplet-laden decaying homogeneous isotropic turbulence (HIT) produced by Dodd & Ferrante (2016). These simulations used the VoF method to resolve the flow inside and outside the droplets and accounted for surface tension effects. A full description of the numerical methods that were used to simulate this flow is offered by Baraldi *et al.* (2014) and Dodd & Ferrante (2014).

3.1. *Initial conditions and droplet properties*

Table 1 shows the dimensionless flow parameters at different times t for the droplet-free flow (case A): ℓ and τ_ℓ are the integral length and timescales; Re_ℓ is the Reynolds number based on ℓ; λ is the Taylor length scale; and η and τ_η are the Kolmogorov length and timescales. The values of the reference length and velocity scales used in normalizing the above quantities were $\tilde{L}_{ref} = 2.43 \times 10^{-3}$ m and $\tilde{U}_{ref} = 110$ m s^{-1}, which, together with the Reynolds number Re, produce the appropriate value of the dimensional kinematic viscosity $\tilde{\nu}_{ref} = 4.16 \times 10^{-6}$ m^2 s^{-1} of the fluid at high temperature ($T_{ref} = 800$ K) and pressure ($p_{ref} = 20$ bar) relevant to gas turbine settings. These reference quantities yield dimensional values for the r.m.s. velocity and droplet diameter at injection time ($t = 1$) of $\tilde{U}_{\mathrm{rms}} = 5.03$ m s^{-1} and $\tilde{D}_0 = 75$ μm, respectively. The smallest scales of turbulence are well resolved, as indicated by $\eta\kappa_{\max} \geq 1$ at all times, where $\kappa_{\max} = \pi N$ is the maximum resolved wavenumber and $N = 1024$ is the number of grid points in each direction of the computational grid.

We perform one simulation (case A) of droplet-free flow and eight simulations (A*–H) of droplet-laden isotropic turbulence (Table 2). Case A* is a limiting case in which the viscosity and density ratio are unity and the Weber number of the droplets is infinity. We analyze the effects of varying the initial droplet Weber number ($We_{\rm rms} = D_0 U_{\rm rms}^2 \rho_c/\sigma$), where σ is the surface tension coefficient, droplet- to carrier-fluid density ratio ($\varphi = \rho_d/\rho_c$), and droplet- to carrier-fluid viscosity ratio ($\gamma = \mu_d/\mu_c$) in the three sets BCD, CEF, and CGH, respectively, while keeping the other two parameters constant. In cases B, C, and D, $We_{\rm rms}$ increases from 0.1 to 5.0 by decreasing the surface tension coefficient. In cases C, E, and F, φ increases from 1 to 100 by increasing ρ_d. In cases C, G, and H, γ increases from 1 to 100 by increasing μ_d. For all cases, the droplet volume fraction is $\phi_v = 0.05$, the initial number of droplets is $N_d = 3130$, and the initial droplet diameter is $D_0 = 0.03125$, which is $20\eta_1$ (or $1.1\lambda_1$), where η_1 and λ_1 are the Kolmogorov and Taylor length scales, respectively, at the time the droplets are released in the flow ($t = 1$). This yields a droplet resolution of 32 grid points per diameter ($N_{gp,d} = 32$). In this brief, we will primarily focus on case C and leave the effects of varying $We_{\rm rms}$, φ, and γ on the velocity-gradient invariants for future work.

3.2. *Length scales of droplet-laden isotropic turbulence*

In single-phase isotropic turbulence, η characterizes the smallest length scales of the flow. Whether this still holds in isotropic turbulence laden with finite-size droplets depends on the flow and droplet properties. If droplet breakup and coalescence are considered, then thin ligaments and gas films are almost always several orders of magnitude smaller than the smallest length scales of the surrounding flow. In the present flow, breakup and coalescence events are minimized by keeping the Weber number order at unity and the droplet volume fraction relatively low (5%).

The other length scale that could be smaller than η is the one associated with the large velocity gradients that develop at the interface between the droplet and carrier fluid. We can obtain a conservative estimate of the thickness of this transition region in which viscous effects dominate if we assume its thickness to be equal to the thickness of the boundary layer on a rigid sphere immersed in a uniform flow. This estimate is conservative because, compared to rigid spheres, droplets develop internal circulation in the direction of the free-stream flow, which effectively lowers the free-stream velocity (U_∞) and thus increases the boundary-layer thickness.

To estimate the nominal boundary-layer thickness of the droplet, we model the droplet as a rigid sphere in uniform flow, in which the free-stream velocity is the r.m.s. velocity of the turbulence. This approximation is reasonable given that the droplet diameter is roughly one-third as large as than the integral scale of turbulence ($\ell/D_0 = 3.3$); therefore, the energy-containing scales, as seen by the droplet, are relatively large compared to its size. We find an approximate laminar boundary-layer solution for the sphere by numerically solving the momentum integral equation for arbitrarily varying free-stream velocity over a body of revolution. Taking the free-stream velocity of $U_\infty = 0.0397$, the calculated boundary-layer thickness at the forward stagnation point ($\theta = 0$, where the boundary layer is thinnest) is $\delta_{99} = 0.0036$, and near the separation point ($\theta = 90^\circ$) it is $\delta_{99} = 0.0068$. The average boundary-layer thickness over the leading surface is $\bar{\delta}_{99} = 0.0044$, which, in terms of the initial droplet diameter, gives $D_0/\bar{\delta}_{99} = 7.1$. This value for $\bar{\delta}_{99}$ should be taken as a rough estimate of the mean boundary-layer thickness on the droplets since we are neglecting droplet shape effects, nonuniform and unsteady flow effects, and droplet internal circulation. Nevertheless, the DNS results will show

t	$U_{\rm rms}$	ε	ℓ	λ	η	Re_ℓ	Re_λ	ℓ/η	τ_ℓ	τ_λ	τ_η
0.0	0.0509	$1.15e-3$	0.0965	0.0229	$1.35e-3$	316	75.0	71.7	1.89	0.45	0.116
1.0	0.0457	$6.10e-4$	0.1038	0.0283	$1.58e-3$	305	83.1	65.8	2.27	0.62	0.160
2.5	0.0397	$4.49e-4$	0.1030	0.0286	$1.70e-3$	262	72.3	60.5	2.60	0.72	0.186
6.0	0.0285	$2.18e-4$	0.1082	0.0295	$2.04e-3$	198	54.0	53.0	3.80	1.04	0.268

TABLE 1. Flow parameters (dimensionless) at initial time ($t = 0$), droplet release time ($t = 1$), time at which tensor invariants are computed ($t = 2.5$), and final time ($t = 6$) in case A.

Case	$We_{\rm rms}$	$\varphi \equiv \rho_d/\rho_c$	$\gamma \equiv \mu_d/\mu_c$	τ_d	τ_d/τ_ℓ	τ_d/τ_η	ϕ_m	ϕ_v	We
A	–	–	–	–	–	–	0	0	–
A*	∞	1	1	–	–	–	0.05	0.05	∞
B	0.1	10	10	35.9	15.8	225	0.5	0.05	1.53×10^3
C	1.0	10	10	35.9	15.8	225	0.5	0.05	1.53×10^4
D	5.0	10	10	35.9	15.8	225	0.5	0.05	7.65×10^4
E	1.0	1	10	3.59	1.58	22.5	0.05	0.05	1.53×10^4
F	1.0	100	10	359	158	2250	5.0	0.05	1.53×10^4
G	1.0	10	1	41.8	18.4	261	0.5	0.05	1.53×10^4
H	1.0	10	100	34.9	15.4	219	0.5	0.05	1.53×10^4

TABLE 2. Droplet properties (dimensionless) at release time ($t = 1$).

that $\bar{\delta}_{99}$ accurately demarcates the transition from boundary-layer-like flow topologies to those characteristic of HIT.

3.3. *Conditional averaging methodology*

Motivated by investigating the flow topologies near the droplet surface, we introduce a conditional averaging procedure to compute statistical quantities conditioned on distance from the interface. Starting with the VoF field, we use the marching cubes algorithm to construct a signed distance function representing the shortest distance to the interface, which has the property $\phi = 0$ at the interface, $\phi < 0$ in the droplet fluid, and $\phi > 0$ in the carrier fluid. Figure 1 shows the VoF and LS fields in an x–y plane at the time when the tensor invariants are computed ($t = 2.5$). Note that the computational cost of the algorithm to compute ϕ for a given C scales as $(|\phi|_{\max}N)^3$, where $|\phi|_{\max}$ is the maximum search distance for computing ϕ and N is the number of grid points in each spatial direction. Therefore, to limit computational cost while adequately capturing the boundary-layer region, we set $|\phi|_{\max}$ to approximately one droplet diameter D_0. This limitation explains the white regions in Figure 1(b).

4. Results

4.1. *Conditionally averaged dissipation rate*

The introduction of finite-size droplets into HIT increases the decay rate of TKE relative to droplet-free flow (Dodd & Ferrante 2016). By comparing the relative magnitudes of

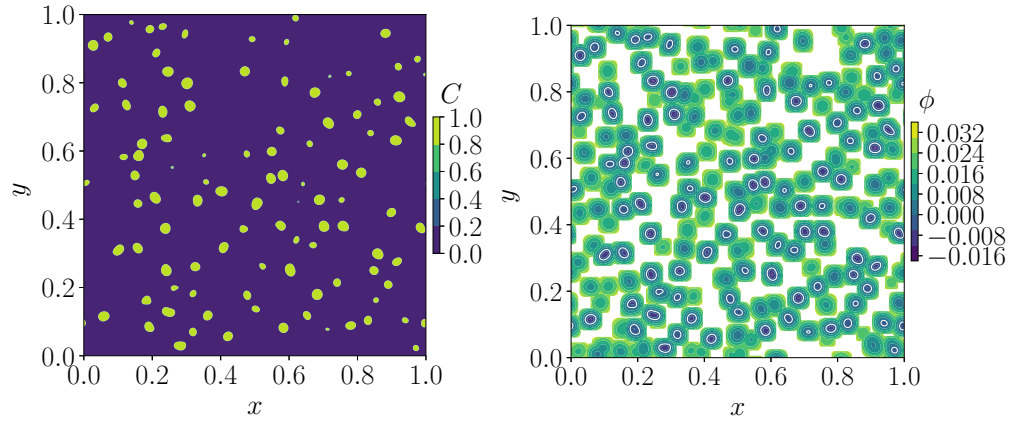

(a) (b)

FIGURE 1. Instantaneous contours in the x–y plane of (a) the VoF field, $C = C(\mathbf{x}, t)$, and (b) the level-set field, $\phi = \phi(\mathbf{x}, t)$, for case C at $t = 2.5$.

the terms in the carrier-fluid TKE budget equation

$$\frac{\mathrm{d}k_c(t)}{\mathrm{d}t} = -\varepsilon_c(t) + T_{\nu,c}(t) + T_{p,c}(t), \tag{4.1}$$

where $\varepsilon_c(t)$ is the dissipation rate of TKE, $T_{\nu,c}(t)$ is the viscous power, and $T_{p,c}(t)$ is the pressure power, DNS has shown that the enhanced decay rate of k_c was primarily caused by an increase in magnitude of ε_c. By analyzing contours of the local dissipation rate in the presence of the droplets, it was observed that the dissipation rate was enhanced near the droplet interface, explaining the increase in the magnitude of $\varepsilon_c(t)$.

To better quantify the enhanced dissipation of TKE near the interface, we condition $\varepsilon' \equiv Re^{-1}(T_{ij}S_{ij})$ on ϕ using the method described in Section 3.3. Figure 2 shows the conditional dissipation rate, $\langle\varepsilon'|\phi\rangle$, as a function of distance from the interface, ϕ, and normalized by the dissipation rate at $t = 1$, ε_1, for all cases. When computing the conditional mean, we only include those statistics in which there are at least one million samples, which has been shown to yield statistically converged results (Dodd & Ferrante 2016). Note that in case A* ($We = \infty$), the interface is a fluid tracer surface; therefore, as the flow evolves, the interface area increases substantially due to strain, so the probability of finding a point at some distance from the interface decreases in time. This explains, in part, why the domain of $\langle\varepsilon'|\phi\rangle$ in case A* decreases in time and is less than for the finite-Weber-number cases.

Figure 2 shows that in the droplet-laden cases (B–H) $\langle\varepsilon'|\phi\rangle$ is maximum at the interface ($\phi = 0$) for all times. In fact the dissipation rate at $\phi = 0$ on both the droplet-fluid and carrier-fluid sides of the interface is several times larger than the rate far away from the interface $|\phi/D_0| > 0.2$. In addition, in the cases of highest Weber number (case B in Figure 2(b)) and highest viscosity ratio (case H in Figure 2(h)), $\langle\varepsilon'|\phi\rangle$ is always an order of magnitude larger at the interface than away from the interface. Because the dissipation enhancement persists in time and is markedly higher than in case A*, it suggests that this effect is not a result of the initial condition of setting the initial droplet velocity to zero, but rather robust. The enhanced dissipation near the interface is result of an increase in the velocity gradient $\partial u_i/\partial x_j$. This is caused by the droplet Stokes number based on

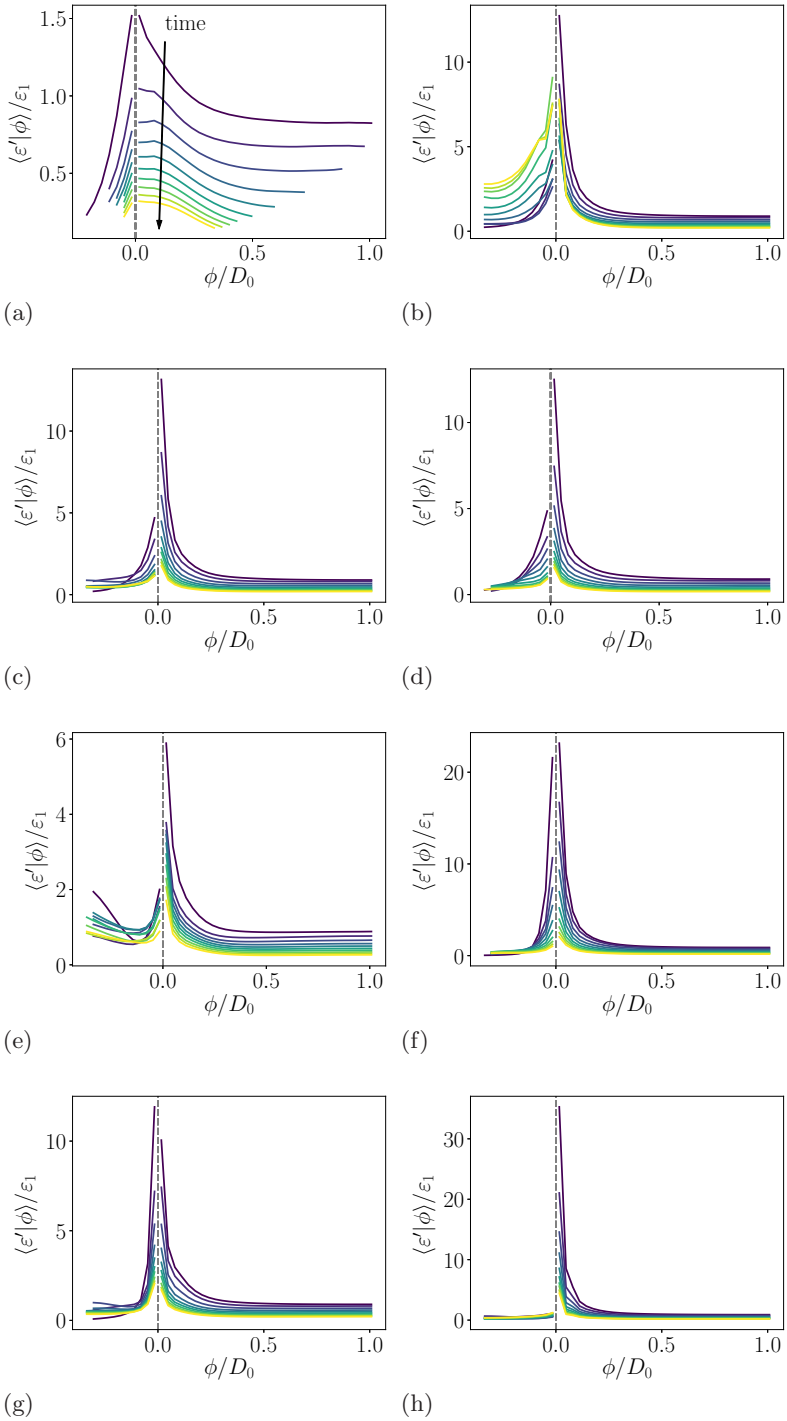

FIGURE 2. Dissipation rate conditionally averaged on distance from the interface ($\langle\varepsilon'|\phi\rangle$) for (a)–(h) cases A* to H and various times from $t = 1$ to 6. The intensity of the line decreases as time increases as indicated in (a).

both the Kolmogorov and integral timescales (τ_d/τ_η and τ_d/τ_ℓ) being much larger than unity; consequently, the droplet motion deviates from the carrier-fluid turbulent eddies. Due to the continuity condition that $\mathbf{u}_c = \mathbf{u}_d$ at the interface, the carrier-fluid velocity $\mathbf{u}_c$ at $\phi = 0$ is strongly influenced by the droplet motion.

4.2. *Joint PDFs of tensor invariants: effect of distance from the interface*

In this section we present the invariants of the velocity-gradient tensor in the carrier fluid for case C and investigate how the topology of the turbulence changes as the droplet interface is approached. The tensor invariants are computed at every point in the flow using second-order central differences, except near the interface, where the central difference stencil would lead to mixing droplet- and carrier-fluid velocities. In that scenario, a second-order one-sided scheme is used. We then conditionally average these invariants on ϕ and compute the joint PDFs of the invariants.

We normalize the velocity gradient using viscous scales as follows. We first compute the mean interfacial shear stress

$$\tau_I = \left\langle \sqrt{\left(\mathbf{t}_1 \cdot 2\mu\mathbf{S}\cdot\mathbf{n}\right)^2 + \left(\mathbf{t}_2 \cdot 2\mu\mathbf{S}\cdot\mathbf{n}\right)^2} \right\rangle_I, \tag{4.2}$$

where $\mathbf{t}_1$ and $\mathbf{t}_2$ are two orthogonal unit vectors that are tangent to the droplet surface, $\mathbf{n}$ is the unit normal, and the brackets $\langle \ldots \rangle_I$ denote ensemble averaging over all interfacial points. Note that in the absence of surface tension gradients (i.e., no Marangoni stresses), the shear stress is continuous across the interface; i.e., $\tau_I = \tau_{I,c} = \tau_{I,d}$. Next, the friction velocity

$$u_\tau \equiv \sqrt{\frac{\tau_\mathrm{I}}{\rho}} \tag{4.3}$$

and viscous length scale

$$\delta_\nu \equiv \nu\sqrt{\frac{\rho}{\tau_\mathrm{w}}} = \frac{\nu}{u_\tau} \tag{4.4}$$

are defined in the usual manner. Finally, using δ_ν and u_τ the distance ϕ and velocity gradient tensor $\mathbf{A}$ are normalized in terms of wall units as

$$\phi^+ \equiv \frac{\phi}{\delta_\nu}, \quad \mathbf{A}^+ \equiv \frac{\delta_\nu \mathbf{A}}{u_\tau}. \tag{4.5}$$

The values of u_τ and $\delta_{\nu,c}$ are reported in Table 3 for all cases. It is important to note that the ratio $\delta_{\nu,c}/\eta$ for case A* is close to the theoretical value of $\delta_\nu/\eta = (15/4)^{1/4} \approx 1.39$ for isotropic turbulence, where τ_w is defined as $\tau_w \equiv \mu[2\langle(\partial u_1/\partial x_2)^2\rangle]^{1/2}$. This again suggests that the effect of initial conditions does not persist, and canonical decaying isotropic turbulence is observed at $t = 2.5$. If we compare $\delta_{\nu,c}/\eta$ for case A* to the droplet-laden cases B–H, $\delta_{\nu,c}/\eta$ for the droplet-laden cases is consistently one-third to one-half as large. This finding indicates that, for the cases considered here, the computational cost of DNS of finite-size droplets in turbulence is substantially higher (2^3–3^3 times higher in terms of the number of grid points) compared to single-phase isotropic turbulence.

The joint PDFs are computed in four different layers on the basis of the distance from the interface at $0 \le \phi^+ \le 1$, $1 \le \phi^+ \le 2$, $4 \le \phi^+ \le 5$, and $9 \le \phi^+ \le 10$, which we will term the $\phi^+ = 1$, 2, 5, and 10 layers, respectively. Figure 3 shows the joint PDFs of Q_A^+ versus R_A^+, Q_S^+ versus R_S^+, and $-Q_S^+$ versus Q_Ω^+ conditionally averaged on the different layers. The joint PDF of Q_A^+ versus R_A^+ in the $\phi^+ = 10$ layer shows that the most probable flow topologies are in the upper left ($Q_A^+ > 0$ and $R_A^+ < 0$)

Case	τ_I	$u_{\tau c}$	$\delta_{\nu c}$	$\delta_{\nu c}/\eta$
A*	4.85×10^{-5}	6.96×10^{-3}	2.24×10^{-3}	1.42
B	2.45×10^{-4}	1.57×10^{-2}	9.94×10^{-4}	0.630
C	2.41×10^{-4}	1.55×10^{-2}	1.00×10^{-3}	0.636
D	2.33×10^{-4}	1.53×10^{-2}	1.02×10^{-3}	0.647
E	1.77×10^{-4}	1.33×10^{-2}	1.17×10^{-3}	0.741
F	3.40×10^{-4}	1.84×10^{-2}	8.45×10^{-4}	0.535
G	1.40×10^{-4}	1.18×10^{-2}	1.31×10^{-3}	0.833
H	3.40×10^{-4}	1.84×10^{-2}	8.45×10^{-4}	0.536

TABLE 3. Viscous scaling parameters at $t = 2.5$: shear stress at the interface, τ_I, and friction velocity, $u_{\tau c}$, viscous length scale, $\delta_{\nu c}$, and ratio with η for the carrier phase.

and lower right ($Q_A^+ < 0$ and $R_A^+ > 0$) quadrants, indicating that the most likely flow topologies are stable focus/stretching and unstable node/saddle/saddle (Chong *et al.* 1990). Topologies corresponding to ($Q_A^+ > 0$ and $R_A^+ < 0$) represent high enstrophy, vortical motions that contribute to the production of enstrophy via vortex stretching. When $Q_A^+ < 0$ and $R_A^+ > 0$, this is indicative of regions of high strain/dissipation that are undergoing compression in one direction and extension in the two other directions (biaxial strain). The particularly inclined teardrop shape and self-similarity of the joint PDF shown in Figure 3(a) closely resemble those found in single-phase homogeneous isotropic turbulence (Ooi *et al.* 1999) as well as various inhomogeneous turbulent flows (Sondergaard *et al.* 1991; Soria *et al.* 1994; Blackburn *et al.* 1996). This suggests that for $\phi^+ \geq 10$, the small-scale motions closely follow the universal properties of single-phase turbulence and that the modulation of turbulence by the droplets is undetected by looking at the fine-scale motions.

The sequence of Figure 3(a,d,g,j), shows the joint PDFs of Q_A^+ versus R_A^+ as the interface is approached. By comparing lines of constant probability density, the results show that the magnitudes of Q_A^+ and R_A^+ increase monotonically from the layers at $\phi^+ = 10$ to $\phi^+ = 1$, meaning that, on average, the magnitude of the velocity gradients increases as the interface is approached. This is consistent with the droplets' inertia causing their trajectories to deviate from the carrier fluid and leading to increased velocity gradients. The shape of the joint PDFs departs from teardrop and becomes more symmetric with respect to the line $R_A^+ = 0$, presenting the highest probabilities at $Q_A^+ = 0$ and $R_A^+ = 0$.

Events clustered at $Q_A = 0$ and $R_A = 0$ are indicative of boundary-layer-like flow topologies (Blackburn *et al.* 1996). To see this, consider $\mathbf{A}$ in a planar boundary-layer flow. Without loss of generality, the interface is oriented such that the interface normal is aligned with the y axis and the velocity is aligned with the x axis, such that at the droplet surface the velocity-gradient tensor, to leading order (Schlichting 1979), is

$$A_{ij} = \begin{bmatrix} 0 & \frac{\partial u}{\partial y} & 0 \\ 0 & 0 & 0 \\ 0 & 0 & 0 \end{bmatrix}. \tag{4.6}$$

The invariants of Eq. (4.6) are $Q_A = R_A = 0$, $Q_S = (\partial u/\partial y)^2/4$, $R_S = 0$, and $Q_\Omega = -Q_S$.

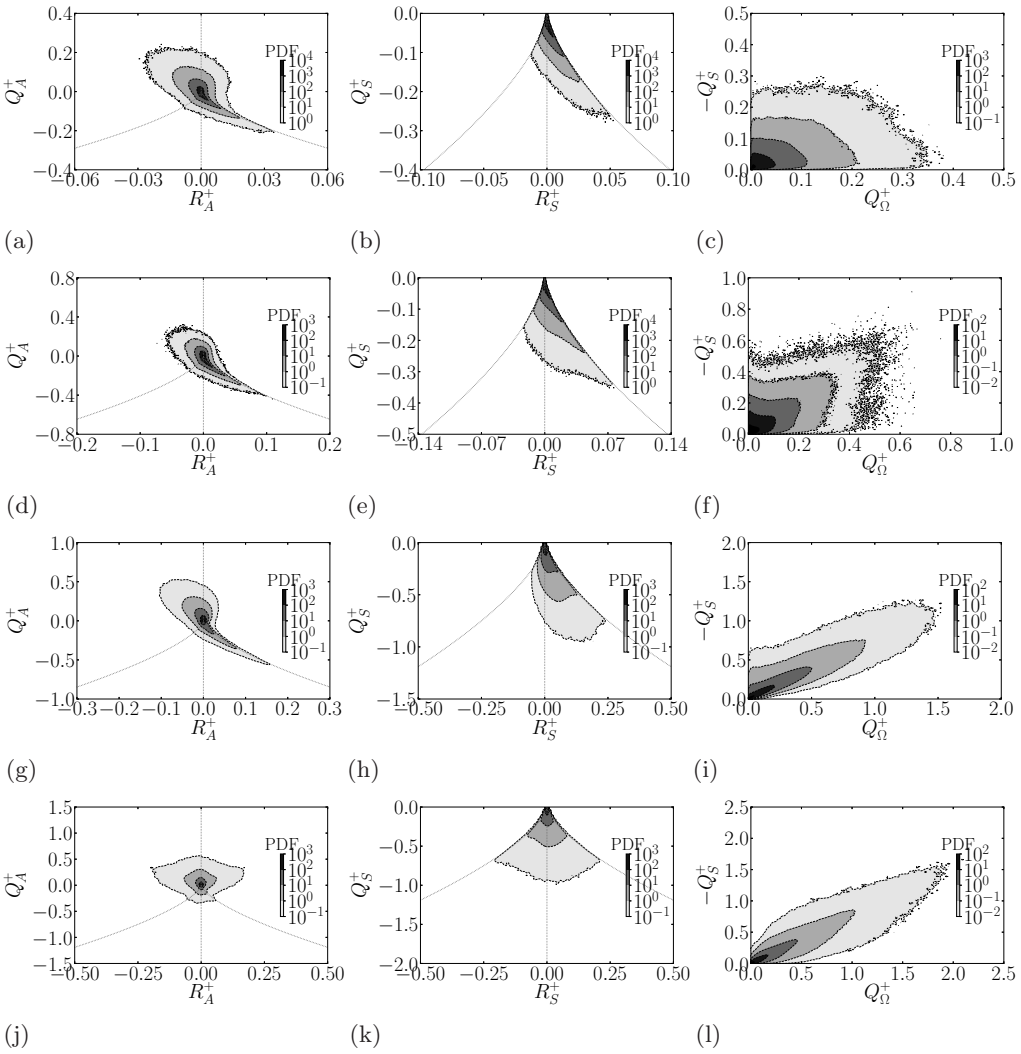

FIGURE 3. Joint PDFs of (a,d,g,j) Q_A^+ versus R_A^+, (b,e,h,k) Q_S^+ versus R_S^+, and (c,f,i,l) $-Q_S^+$ versus Q_Ω^+ conditioned on different distances from the interface: (a–c) $\phi^+ = 10$, (d–f) $\phi^+ = 5$, (g–i) $\phi^+ = 2$, and (j–l) $\phi^+ = 1$.

It is perhaps not surprising then that the symmetry about $R_A^+ = 0$ and clustering near the origin were also reported by Blackburn *et al.* (1996) in turbulent channel flow.

Figure 3(b,e,h,k) shows the joint PDFs of Q_S^+ versus R_S^+ for the four layers near the interface. Farthest from the interface, Figure 3(b) shows that the PDF is skewed toward $R_S^+ > 0$, with most of the events attracted to the line $27R_S^2 + 4Q_S^3 = 0$. Along this line, the principal rates of strain are in the ratio $\lambda_1 : \lambda_2 : \lambda_3 = 1 : 1 : -2$; therefore, the flow is expanding in two directions and contracting in the third direction, forming disk-like structures, which tend to be associated with the formation of vortex sheets. A comparison of Figure 3(b,e,h,k), shows that the flow becomes less skewed toward the biaxial straining topologies as ϕ decreases. At the droplet interface, there is equal probability of finding

biaxial ($R_S^+ > 0$) and axial ($R_S^+ < 0$) strain fields, and the most likely events appear to lie along the line $R_S^+ = 0$. The clustering along $R_S^+ = 0$ is consistent with the invariants for $\mathbf{A}$ in a planar boundary layer as shown in Eq. (4.6). The increasing preference for $R_S^+ = 0$ events as the interface is approached is also in agreement with the behavior of Q_S and R_S reported in turbulent channel flow as the distance to the wall decreases.

We now look at the joint PDFs of Q_S^+ and Q_Ω^+ shown in Figure 3(c,f,i,l). At the distance farthest from the droplet surface ($\phi^+ = 10$), shown in Figure 3(c), the PDF is skewed toward small-scale motions with low dissipation and high enstrophy ($Q_\Omega^+ > -Q_S^+$). This is explained by the fact that motions with high enstrophy are solid-body rotations and therefore persist for a longer time than straining motions (Ooi *et al.* 1999). The shape of the joint PDF in Figure 3(c) is in good agreement with that found in single-phase isotropic turbulence and more complex turbulent flows. As ϕ decreases, the magnitude of the invariants increases by nearly an order of magnitude, indicating that both the mean enstrophy and dissipation rate increase substantially as the droplet surface is approached. Interestingly, as ϕ^+ changes from 10 to 5 in Figure 3(c,f), the PDF goes from being skewed toward $Q_S^+ = 0$ to $Q_\Omega^+ = 0$. This signals that outside the boundary layer, there is a preference for vortical motions, as previously mentioned, but inside the droplet boundary layer, highly dissipative flow topologies are prevailing.

Moving further into the boundary layer from $\phi^+ = 5$ to $\phi^+ = 2$ and 1, shown in Figure 3(i,l), the distribution of Q_S^+ and Q_Ω^+ clusters along the line $Q_\Omega = -Q_S$, corresponding to vortex sheet structures. This preference for $Q_\Omega = -Q_S$ was also observed in the buffer and viscous regions of a turbulent boundary layer (Blackburn *et al.* 1996).

5. Conclusions

This work reports the joint PDFs of the invariants of the velocity-gradient, rate-of-strain, and rate-of-rotation tensors in decaying isotropic turbulence laden with finite-size droplets ($D_0/\eta = 20$). The joint PDFs were computed in the carrier phase for different distances from the interface using a novel conditional averaging procedure. Four distinct regions of local flow topology can be identified in the vicinity of the droplet interface:

(*a*) An outer region ($\phi > \delta$) where the flow topologies show a preference for stable focus/stretching ($Q_A > 0$ and $R_A < 0$) and unstable node/saddle/saddle ($Q_A < 0$ and $R_A > 0$) topologies that closely resemble canonical isotropic turbulence.

(*b*) A transition region ($\phi \approx \delta$) marked by a shift in the skewness of the joint PDF of Q_Ω and $-Q_S$ from a preference for high enstrophy/low dissipation ($Q_\Omega > -Q_S$) to high dissipation/low enstrophy ($-Q_S > Q_\Omega$). The transition is also apparent in the joint PDFs of Q_A versus R_A, which show a marked increase in density along the so-called Vieillefosse tail, the region of Q–R space where strain production is highest.

(*c*) An inner region ($\phi < \delta$, $\phi^+ > 1$) denoted by an increased density for $Q_\omega = -Q_S$, which is characteristic of boundary-layer flows and vortex sheets.

(*d*) A viscous wall region dominated by boundary-layer-like flow topologies leading to clustering at $Q_A = 0$ and $R_A = 0$. The probability of axial and biaxial straining motions becomes equal, as denoted by symmetry in the Q_S versus R_S PDF about the line $R_S = 0$.

Accurately capturing the velocity gradient near the droplet interface is crucial for the accurate prediction of the dissipation rate of TKE as well the viscous coupling force between the carrier and droplet phases. Inadequate numerical resolution in DNS or inaccurate subgrid-scale models in an LES framework will lead to incorrect turbulent energetics and droplet dynamics. The similarities between the small-scale flow topologies

in droplet-laden isotropic turbulence and turbulent wall flows suggest that models in the latter could be applied or adapted to the former. A possible modeling paradigm would resolve the smallest length scales of the bulk flow, use reduced resolution to capture the droplet interface (e.g., $N_{gp,d} = 8$ instead of 32), and apply a wall model to accurately predict the shear stress induced by the droplet.

Acknowledgments

This study was supported by the Office of Naval Research (ONR), Grant No. N00014-15-1-2726. This work used the Extreme Science and Engineering Discovery Environment (XSEDE), which is supported by the National Science Foundation (NSF), Grant No. ACI-1548562. In particular, the authors acknowledge the Texas Advanced Computing Center (TACC) at The University of Texas at Austin through allocation TG-CTS180029 for providing high-performance computing resources that have contributed to the research results reported within this paper.

REFERENCES

Baraldi, A., Dodd, M. S. & Ferrante, A. 2014 A mass-conserving volume-of-fluid method: volume tracking and droplet surface-tension in incompressible isotropic turbulence. *Comput. Fluids* **96**, 322–337.

Blackburn, H. M., Mansour, N. N. & Cantwell, B. J. 1996 Topology of fine-scale motions in turbulent channel flow. *J. Fluid Mech.* **310**, 269–292.

Chong, M. S., Perry, A. E. & Cantwell, B. J. 1990 A general classification of three-dimensional flow fields. *Phys. Fluids A* **2**, 765–777.

Dodd, M. S. & Ferrante, A. 2014 A fast pressure-correction method for incompressible two-fluid flows. *J. Comput. Phys.* **273**, 416–434.

Dodd, M. S. & Ferrante, A. 2016 On the interaction of Taylor lengthscale size droplets and isotropic turbulence. *J. Fluid Mech.* **806**, 356–412.

Ooi, A., Martin, J., Soria, J. & Chong, M. 1999 A study of the evolution and characteristics of the invariants of the velocity-gradient tensor in isotropic turbulence. *J. Fluid Mech.* **381**, 141–174.

Schlichting, H. 1979 *Boundary-Layer Theory*. McGraw-Hill, New York.

Sondergaard, R., Chen, J., Soria, J. & Cantwell, B. 1991 Local topology of small scale motions in turbulent shear flows. In *8th Symposium on Turbulent Shear Flows*, pp. 1–16. Munich, Germany.

Soria, J., Sondergaard, R., Cantwell, B., Chong, M. & Perry, A. 1994 A study of the fine-scale motions of incompressible time-developing mixing layers. *Phys. Fluids* **6**, 871–884.